Mineralium Deposita (2024) 59:313–328
https://doi.org/10.1007/s00126-023-01211-w

ARTICLE

Lithium and oxygen isotopic constraints on the source and evolution of ore-forming fluids: a case study from the Shuiyindong Carlin-type gold deposit, SW China

Ningning Hu[1,2] · Ruizhong Hu[1,2] · Heng Chen[3] · Shanling Fu[1] · Jiehua Yang[1] · Lin Xu[4] · Chongguang Luo[1]

Received: 4 January 2023 / Accepted: 4 September 2023 / Published online: 21 September 2023

Abstract

Carlin-type gold deposits are among the most important gold-bearing hydrothermal ore systems and are mainly located in Nevada, USA, and southwestern China. However, the source and evolution of the ore-forming fluids for these deposits remain controversial, especially those found within China. In this study, lithium and oxygen isotopic analyses of quartz-hosted fluid inclusions are used to elucidate the source and evolution of the giant Shuiyindong Carlin-type gold deposit. Fluid inclusions trapped in quartz of three distinct genetic stages have low salinity (0.8–6.3wt% NaCl equiv.) and moderate temperature (154–343 °C), but display variable Li and O isotope signatures. The Li and O isotopes of stage I fluids (δ^7Li values from + 5.1 to + 9.1‰; δ^{18}O values from + 6.3 to + 10.0‰) indicate predominantly a magmatic source for the initial ore-forming fluids. The large variations of Li and O isotopes of stage II fluids (δ^7Li values from + 9.3 to + 16.0‰; δ^{18}O values from + 0.1 to + 7.7‰) suggest that the fluids are controlled by mixing of magmatic fluids and meteoric water, which in turn triggered the precipitation of gold-bearing sulfides. The isotopic compositions of stage III fluids (δ^7Li values from + 15.5 to + 22.8‰; δ^{18}O values from − 5.4 to − 2.8‰) confirm that the final fluids are dominated by meteoric water. Furthermore, this work demonstrates that the combined Li–O isotopic analysis of fluid inclusions is a powerful tracer to decode the source and evolution of ore-forming fluids in hydrothermal mineralizing systems.

Keywords Lithium-oxygen isotopes · Fluid inclusion · Fluid source and evolution · Shuiyindong Carlin-type gold deposit

Introduction

Carlin-type gold deposits are among the most important gold resources and are mainly located in Nevada, USA, and southwestern China (Silliton and Bonham 1990; Hofstra et al. 1991; Hu et al. 2002, 2017). Carlin-type gold deposits are commonly hosted by sedimentary rocks with proximal and rare magmatic rocks. This spatial and temporal relationship between mineralization and magmatism is commonly used to imply a genetic link between the mineralizing fluids and felsic magmatism (Hedenquist and Lowenstern 1994). However, the source and detailed fluid evolution of ore-forming fluids for the Carlin-type gold deposits remain controversial (Emsbo et al. 2003; Cline et al. 2005; Muntean et al. 2011; Hu et al. 2002, 2017; Large et al. 2016; Su et al. 2018; Xie et al. 2018; Jin et al. 2020). The debate is complicated by studies that show overprinting of primary source compositions by late-stage water–rock interaction (Su et al. 2009b; Jin et al. 2020). Several sources were proposed for the Carlin-type gold deposits in SW China, such as presumed magmatic fluids exsolved from concealed magmas (Hou et al. 2016; Xie et al. 2018), basinal brines (Peng et al. 2014), metamorphic fluids (Su et al. 2018), and meteoric waters which interacted with sedimentary rocks (Hu et al. 2002).

Editorial handling: Y. Li

✉ Ruizhong Hu
huruizhong@vip.gyig.ac.cn

1 State Key Laboratory of Ore Deposit Geochemistry, Institute of Geochemistry, Chinese Academy of Sciences, Guiyang 550081, China

2 College of Earth and Planetary Sciences, University of Chinese Academy of Sciences, Beijing 100049, China

3 Lamont-Doherty Earth Observatory, Columbia University, Palisades, NY 10964, USA

4 State Key Laboratory of Nuclear Resources and Environment, East China University of Technology, Nanchang 330013, Jiangxi, China

The Shuiyindong deposit is the largest gold deposit in SW China with over 263 tonnes Au (total proven reserves for SW China: 1000 tonnes Au), and this deposit shows geological characteristics similar to Carlin-type gold deposit (Hu et al. 2017; Li et al. 2020; Gao et al. 2022). Additionally, this deposit contains abundant hydrothermal quartz, which hosts abundant primary fluid inclusions (FIs) that are easily distinguishable from the transparent matrix. The FIs in quartz can record ore-related information including trace elements concentrations, isotope ratios (e.g., Li and O), and pressure, temperature, and salinity that can be used to decode the source and evolution of ore-forming fluids (Fusswinkel et al. 2013; Large et al. 2016; Rusk et al. 2008; Pettke et al. 2010; Richard et al. 2016).

Lithium (Li) is a lithophile element, behaving moderately incompatible in many magmatic systems, and it is highly mobile during hydrothermal processes and fluid-rock interaction (Halama et al. 2009; Tang et al. 2014). Lithium isotope fractionation has been used to investigate water–rock interaction (Chan et al. 2002; James et al. 2003; Brant et al. 2012). The large mass difference (~ 17%) between ^{6} and ^{7}Li and the large scale of fractionation observed in the upper crust (> 80‰ for δ^{7}Li; Tomascak et al. 2016) also make Li isotope compositions sensitive to fluid sources within the crust (e.g., Chan et al. 1994, 2002; Krienitz et al. 2012; Yang et al. 2015; Richard et al. 2018). It was previously reported that different geochemical reservoirs often contain remarkably distinctive Li isotopic compositions. For example, isotopically heavy Li is typically sourced from seawater (e.g., $\delta^{7}Li = +31‰$ in modern sea water) or brines (James and Palmer 2000; Bottomley et al. 2003; Millot et al. 2007), whereas light Li ($\delta^{7}Li < +5‰$) can be derived from magma-related sources (Nishio et al. 2004; Ryan and Kyle 2004; Tomascak et al. 2008; Pogge von Strandmann et al. 2011). Therefore, Li isotopes have recently been employed to decipher the source and evolution of ore-forming fluids, such as in pegmatite deposits, tungsten deposits, and Pb–Zn deposits (Teng et al. 2006a; Masukawa et al. 2013; Deveaud et al. 2015; Yang et al. 2015; Xu et al. 2018, 2021). The oxygen isotopic system is a traditional but powerful tool for understanding the processes involved in ore formation. It can provide critical information about the physico-chemical conditions of the ore-formation processes (Zheng 1993) and the origin of the fluids (Hou et al. 2001; Li et al. 2022). Unfortunately, it is sometimes hard to distinguish whether the isotopic variations result from water–rock interaction or mixing of different sources if only one isotope system is studied. Different reservoirs on Earth generally show unique Li and O isotopic compositions; therefore, isotopic exchange between fluids and rocks (minerals) as well as mixing between the reservoirs likely results in clear Li and O isotope covariations (Harlaux et al. 2021). Therefore, the combination of Li and O stable isotopes can be a novel indicator for tracing the source and evolution of ore-forming fluids in hydrothermal deposits.

In this study, we identify different stages of ore-related hydrothermal quartz in the Shuiyindong deposit to constrain the source and evolution of ore-forming fluids by Li–O isotopes of quartz-hosted FIs. This work demonstrates that combined Li–O isotopes are a powerful tracer of the source and evolution of ore-forming fluids in Carlin-type gold deposits and also could be employed to other hydrothermal mineralizing systems.

Regional geology

The South China Block, situated between the North China Craton and the Indochina Block, was generated by the amalgamation between the Yangtze Block and Cathaysia Block at about 830 Ma (Zhao et al. 2011). It is connected with the North China Craton to the north by a Triassic collision zone (Qinling–Dabie orogenic belt) and the Indochina Block to the south by the Triassic Song Ma Suture (Li and Li 2007; Cai and Zhang 2009).

The Youjiang basin is on the southwestern margin of the South China Block (Fig. 1) and experienced multiple tectonic events (Du et al. 2009; Wang and Groves 2018). The prototype of the Youjiang basin was formed by largely rifting and passive continental margin sedimentation that resulted from the opening of the Paleo-Tethys in the Devonian to Early Permian (Du et al. 2009). Subsequently, this basin developed gradually as a back-arc basin when the Paleo-Tethys oceanic crust subducted beneath the South China Block during Late Permian, and finally evolved into a foreland basin due to the closure of the Paleo-Tethys Ocean with collision between the Indochina and South China Blocks in the Triassic (Yang et al. 2012; Qiu et al. 2016). The Youjiang basin is bounded by several NW- and NE-trending crustal-scale faults with the Shuicheng-Ziyun fault to the northeast, the Mile-Shizong fault to the northwest, and the Red River fault to the southwest (Wang and Groves 2018). The basin is filled with marine sedimentary successions of Cambrian to Middle Triassic ages (Su et al. 2009a; Hu et al. 2017). The Cambrian and Ordovician strata are locally exposed in some anticline cores. Geographically, a sequence of shallow-water carbonate platforms was deposited in the northwestern part of the basin during the Devonian to Triassic, whereas a sequence of deep-water slope/basin calcareous sandstone, siltstone, and shale was deposited in the southeastern part of the basin (Fig. 1; Du et al. 2013). Igneous rocks exposed in the Youjiang basin dominantly include mafic and felsic dikes with ages of less than 100 Ma (Fig. 1; Liu et al. 2010; Chen et al. 2012; Pi et al. 2017; Zhu et al. 2017). Granites (with emplacement ages of between ~ 100 and 80 Ma) and some granite-related W-Sn polymetallic deposits are mainly exposed in the west, east, and southeastern parts of the basin (Cheng et al. 2009, 2010; Feng et al. 2010).

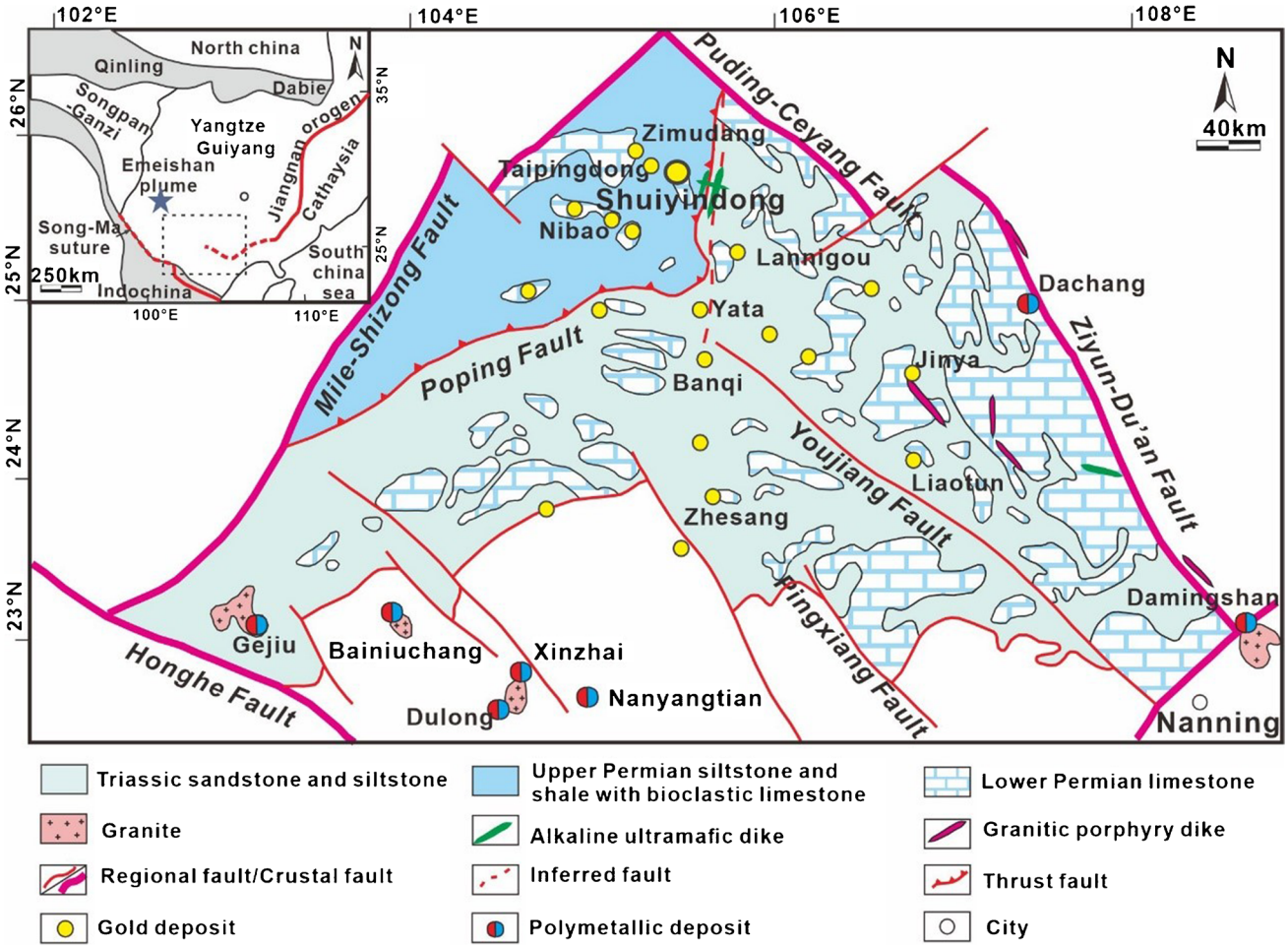

Fig. 1 Regional geological map of the Youjiang Basin in South China showing the location of the Shuiyindong gold deposit (modified after Hu et al. 2017; Gao et al. 2021)

There are many low-temperature hydrothermal deposits (e.g., Au, Sb, Hg) in the Youjiang basin, especially more than 200 Carlin-type gold deposits and occurrences with a total proven reserve of ~ 1000 tonnes Au, such as the Shuiyindong, Zimudang, Lannigou, and Getang gold deposits (Hu et al. 2017; Su et al. 2018). Most of the Carlin-type gold deposits are hosted in Permian and Triassic sedimentary rocks, and the ore bodies can be classified into two types: strata-bound and fault-bound. The fault-bound ore bodies are always hosted in calcareous siltstones and silty mudstones, occurring along high-angle reverse faults, such as the Lannigou, Yata, and Jinya gold deposits. The strata-bound type is mainly hosted in limestone or with mineralization along unconformities, controlled by anticlines or domes, such as in Shuiyindong, Taipingdong, and Getang (Fig. 1). The Carlin-type gold deposits in the Youjiang basin likely formed during two metallogenic episodes at ~ 210 Ma and ~ 140 Ma associated with the late Triassic Indochina orogeny and early Cretaceous subduction of the paleo-Pacific plate, respectively (Gao et al. 2021; Jin et al. 2021).

Deposit geology

The Shuiyindong gold deposit, located at latitude 25°32′ N and longitude 105°31′ E, is one of the best-documented Carlin-type Au deposits in southwestern Guizhou, SW China. The Shuiyindong deposit has proven gold reserves of 263 tonnes with an average gold grade of 5 g/t that makes it the largest deposit in the region (Su et al. 2008, 2009a, b). It was discovered in the 1980s by the No. 105 Geological Team of the Guizhou Bureau of Geology and Mineral Resources, but mining did not begin until 2003. The sedimentary rocks in the Shuiyindong gold deposit consist of the middle Permian Maokou Formation (P_2m), upper Permian Longtan Formation (P_3l), Changxing Formation (P_3c), and Dalong Formation (P_3d) and lower Triassic Yelang Formation (T_1y) and Yongningzhen Formations (T_1yn) (Fig. 2a). The marine sedimentary sequences are dominated by limestones, siltstone, and argillite. The ores are mainly hosted in the Upper Permian Longtan Formation which mainly consists of bioclastic limestone and

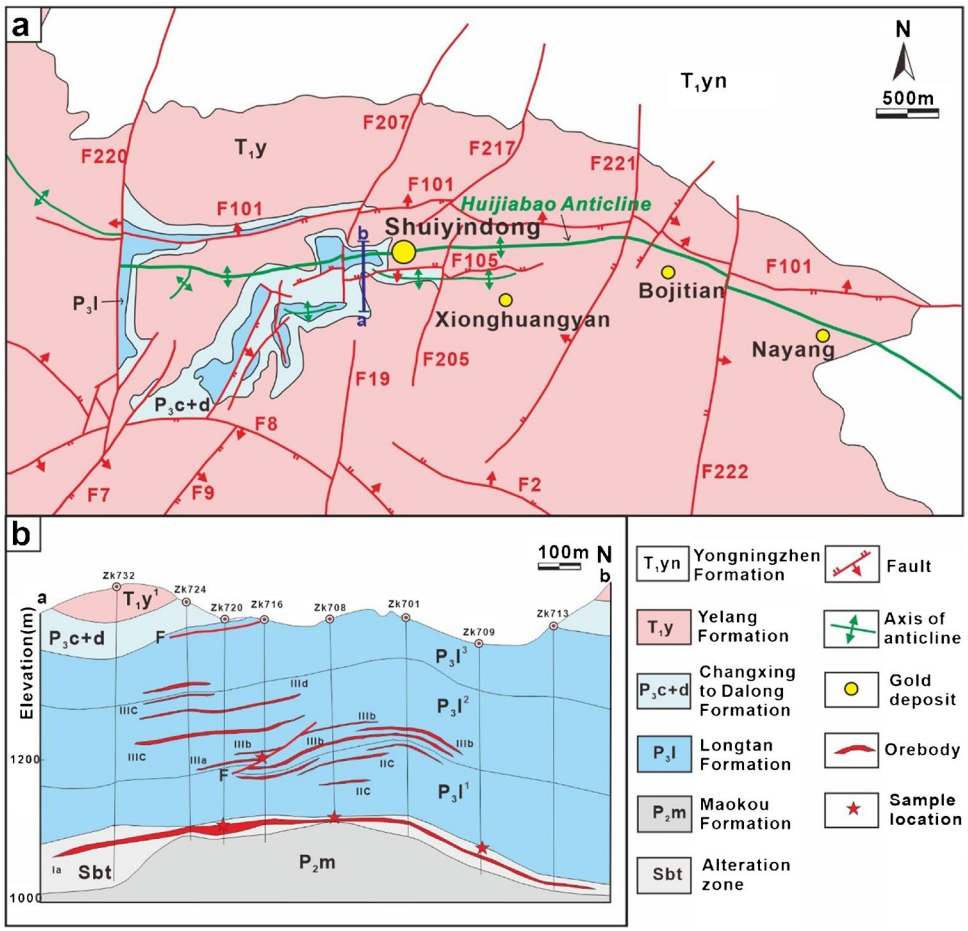

Fig. 2 **a** Structural map of the study area showing the major structural faults and the location of the Shuiyindong gold deposit (modified after Li et al. 2020). **b** Cross section of the Shuiyindong gold deposit (modified after Peng et al. 2014)

calcareous siltstone (Su et al. 2008). Major structures in the Shuiyindong district include the EW-trending Huijiabao anticline and a series of EW-striking faults (e.g., F_{101} and F_{105}). The F_{101} fault dips 50 to 55°N and extends for more than 5.4 km, and the F_{105} dips 45 to 55°S, both of which cut the limbs of the Huijiabao anticline. Additionally, there are NE-trending and NS-trending faults within the anticline. Gold mineralization at the Shuiyindong deposit is strictly confined to the Huijiabao anticline, and the mineralization extends up to 300 m from the axis of the anticline. The fault zones are associated with Au mineralization, and EW-trending major faults may have acted as the structural channels for hydrothermal fluids (Tan et al. 2015b). No surface expression of intrusive rocks has been identified in the deposit, and the nearest igneous rocks (Baiceng alkaline ultramafic dikes) are about 20 km away from this deposit. However, gravity and magnetic data indicate the presence of concealed intrusions underneath the Shuiyindong gold deposit (Liu et al. 2010; Xie et al. 2018).

The gold ore bodies are mainly hosted in the Longtan Formation and generally extend for 100 to 400 m in length and 50 to 350 m in width (Fig. 2b). Stratiform and stratiform-like ore bodies (IIIa, IIIb, IIIc, and IIc) are commonly distributed within the Huijiubao anticline axis. The Ia ore body is hosted in silicified brecciated limestone-argillite between the top of the Maokou Formation and the base of the Longtan Formation. Gold mineralization is closely correlated with hydrothermal alteration, involving decarbonation, sulfidation, silicification, and argillization alteration assemblages. The dominant ore minerals at Shuiyindong are pyrite, arsenopyrite, stibnite, orpiment (As_2S_3), and realgar (As_4S_4). Gangue minerals mainly include quartz, dolomite, calcite, and clay minerals. Most of the gold occurs in arsenic-bearing pyrite (As contents range from 3.37 to 13.32 wt%) as sub-micron particles or lattice gold, while some native gold is also present as grains ranging from 0.1 to 6 μm in size (Su et al. 2008).

The hydrothermal evolution of the Shuiyindong gold deposit can be divided into three stages based on microscopic textural observations, crosscutting relationships, and mineral assemblages (Su et al. 2009b). Stage I is characterized by quartz veins, ranging from 0.5 to 10 cm wide (Fig. 3a–c) that are crosscut by stage II pyrite veins (Fig. 4a–c). Stage II minerals are widespread and economically important and include abundant euhedral arsenic-bearing pyrite, arsenopyrite,

quartz, and dolomite. Coarse-grained euhedral pyrite usually infills cavities developed in decarbonatized limestones with grain size from 20 to 200 μm, while fine-grained euhedral pyrite is commonly intergrown with quartz grains. Stage II quartz veins typically occur in moderately silicified bioclastic limestone, ranging from 0.5 to 20 cm wide (typically 0.5–4 cm) (Fig. 3d–f). Stage III is characterized by an assemblage of pyrite, stibnite, orpiment, realgar, quartz, and calcite. Pyrite in this stage is generally deformed, and quartz veins of this stage crosscut the veins that were deposited in the previous stage (Fig. 3g–i) and stage III quartz veins crosscut the stage II pyrite assemblage (Fig. 4g–i).

Recently, Jin et al. (2021) obtained three U–Pb ages from calcite (204.3 ± 2.0 to 202.6 ± 2.5 Ma, 191.9 ± 2.2 Ma, and 139.3 ± 5.7 to 137.1 ± 9.7 Ma) associated with Au mineralization from the Shuiyindong deposit, and these results indicate that the Shuiyindong deposit formed in the late Triassic and records additional hydrothermal events during the Jurassic and Cretaceous.

Sampling and analytical methods

Sampling strategy and SEM-CL

Samples were mainly collected from underground tunnels or drill hole (Fig. 2). More detailed information about sample locations and lithologies is listed in ESM2 Table S1. Thin sections of each sample are used to examine the paragenetic relations and textural features of the target minerals under the optical microscope. The quartz grains from different stages were handpicked under a binocular microscope after crushing to 20–40 mesh, ultrasonically cleaned in distilled water and dried at room temperature. Quartz was imaged using a JEOL JSM-7800F field emission SEM at the Institute of Geochemistry, Chinese Academy of Sciences (IGCAS) in Guiyang, China. Cathodoluminescence (CL) imaging was performed using an accelerating voltage of 10 kV and a primary beam current of 10 nA.

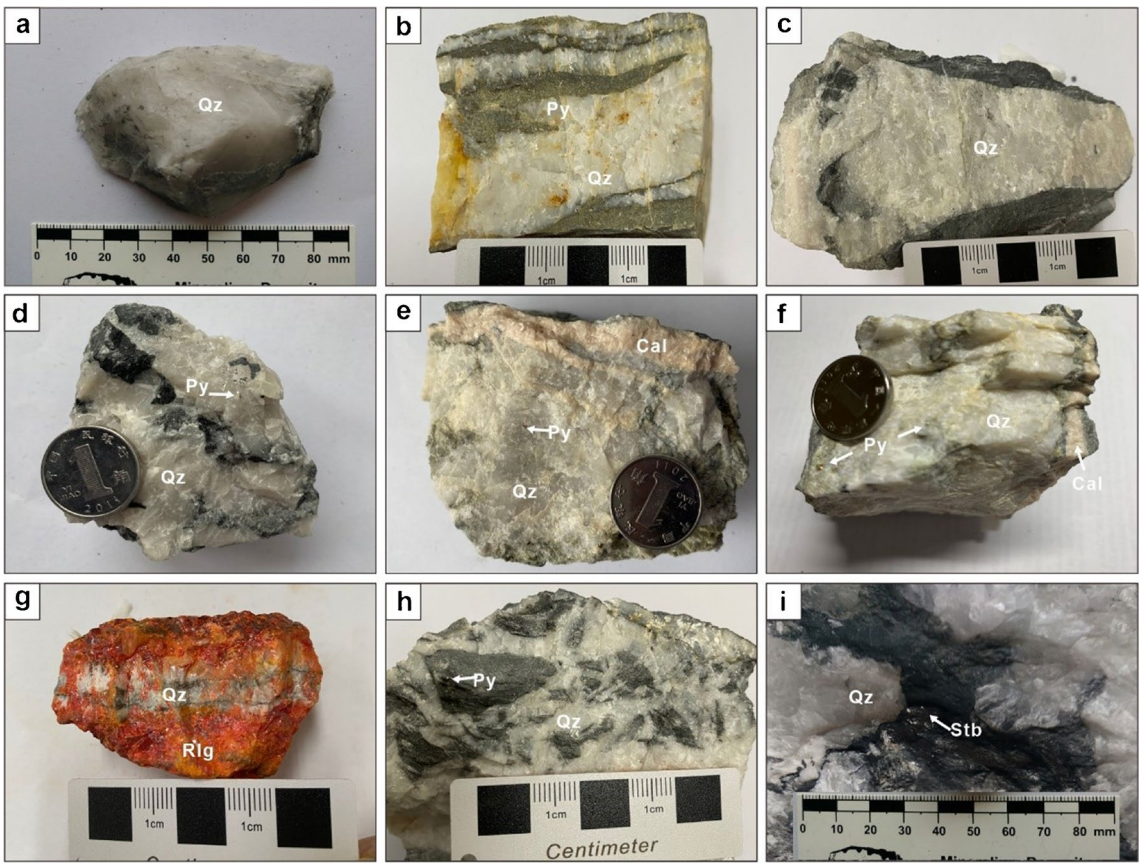

Fig. 3 Photographs of quartz-bearing hand specimens from the Shuiyindong gold deposit. **a**–**c** Quartz vein overprinting pyrite disseminations in silicified bioclastic limestone of stage I. **d** Quartz intergrown with pyrite of stage II. **e**–**f** Quartz intergrown with pyrite of stage II and cut by calcite vein of stage III. **g** Quartz vein associated with realgar of stage III. **h** Stage III quartz vein cutting mineralized silicified limestone breccia. **i** Quartz associated with stibnite of stage III. Abbreviations: Py = pyrite, Qz = quartz, Rlg = realgar, Stb = stibnite, Cal = calcite

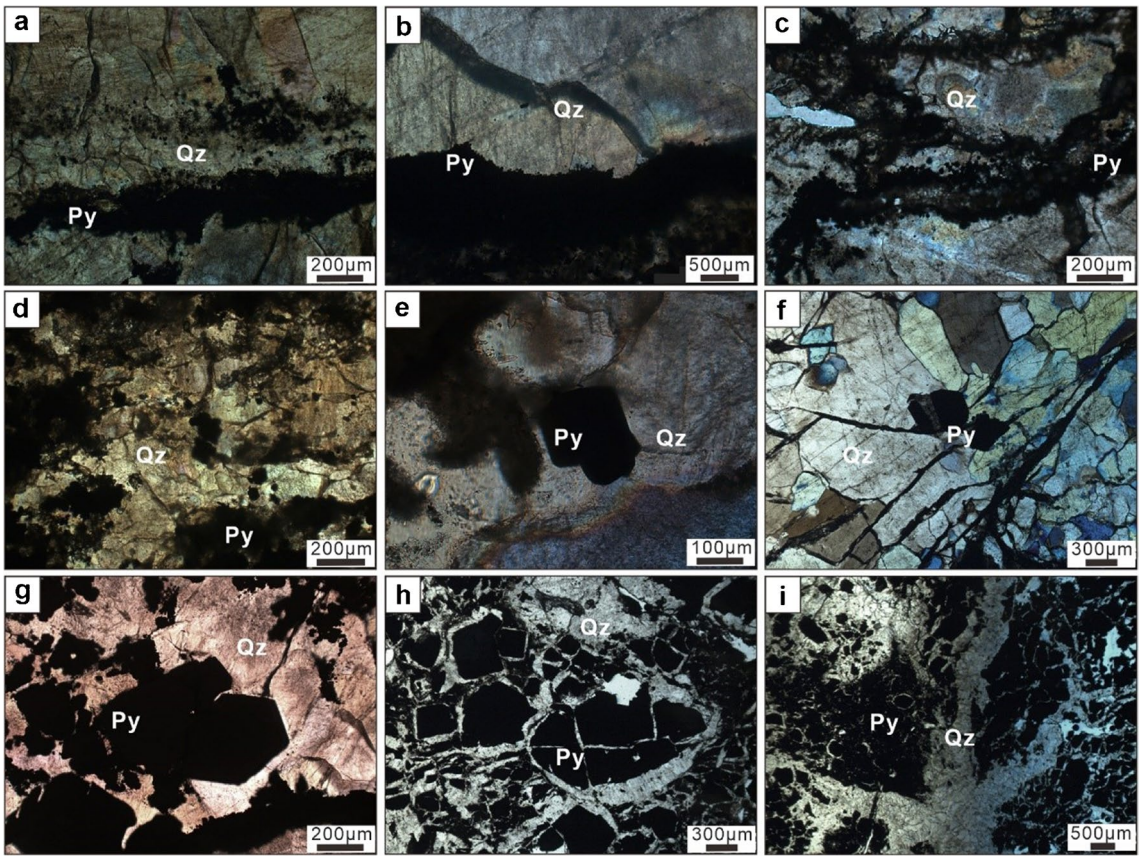

Fig. 4 Photomicrographs showing the mineralogy and textures of quartz from the Shuiyindong gold deposit. **a–c** Pyrite infill along quartz fissure of stage I stage. **d–f** Quartz vein and quartz intergrown with idiomorphic pyrite of stage II. **g–i** Stage III quartz vein cutting stage II pyrite. Abbreviations: Py = pyrite, Qz = quartz

Microthermometry

Doubly-polished sections, approximately 200 μm thick, were prepared for this study. Microthermometry of FIs was measured on a Linkam THMS600 heating-freezing stage with temperature range of − 196 to 600 °C mounted on a Leica microscope, at the IGCAS. The precision of the homogenization temperature (Th) measurements is about ± 2 °C for temperatures above 100 °C. The FIs are analyzed by freezing down to − 120 °C and heating at a rate of 0.5 °C/min. The heating rate is reduced to 0.1 °C/min when near the melting temperature of solid CO_2 (Tm_{CO2}), ice melting temperatures (Tm_{ice}), CO_2 clathrate melting temperatures (Tm_{clath}), and homogenization temperature of the CO_2 (Th_{CO2}). The salinities of aqueous FIs are determined using the equations of Bodnar (1993) for NaCl–H_2O inclusions and Steele-Maclnnis (2018) for CO_2-bearing inclusions.

Li and Cl concentrations

Approximately 5 g of quartz was cleaned in HNO_3 to remove impurities (e.g., calcite) and heated to 150 °C for 2 h to remove the secondary inclusions (based on traditional analysis of primary fluid inclusion that homogenization temperatures are greater than 150 °C; Peng et al. 2014). The powdered samples (50 mg) were dissolved by HF + HNO_3 mixture for 48 h at 190 °C in a high-pressure Teflon bomb, and then, samples were added to 2 mL of 2.0% (v/v) HNO_3 solution for analysis of Li concentrations in quartz. The cleaned quartz grains are grinded with 18.2 MΩ Milli-Q ultrapure water to fine powders (> 200 mesh) using a clean planetary ball mill equipped with agate grinding balls, and then leached (using nylon filters with 0.22-μm pores to remove the quartz powder which is dried for O isotope analysis), and repeatedly washed by Milli-Q ultrapure water to collect the fluid inclusions liberated during grinding. This washing was repeated until the electrical conductivity of the leachates was the same as the Milli-Q ultrapure water. The blank extraction has minor Li content with an average blank (n = 5) of 0.074 ng/g determined on a NexION 300X ICP-MS (ICP-MS).

Lithium concentrations were measured by ICP-MS at the IGCAS. The detection limits and uncertainties are 0.1 ppt and 10%, respectively. The Cl concentrations of the FIs leachates are measured by Dionex ICS-90 ion chromatography (IC) at the IGCAS and with detection limits of approximately 0.05 ppm.

Lithium isotopes

The leachates of FIs are dried and redissolved in 0.5 M HCl before chromatographic separation. The chemical separation uses a two-step liquid chromatography procedure in a super clean lab at IGCAS following the procedure described by Xu et al. (2020). The quartz columns are filled with Dowex 50WX8 resin (200–400 mesh). In the first step, 0.5 M HCl is used as eluent to separate Li from most elements of the sample. In the second step, 0.3 M HCl is used as eluent to purify Li from sodium, resulting in low Na/Li ratio (Na/Li < 0.5). The separation procedure ensured that the Li recovery of all samples was greater than 99% and the column blank less than 0.005% of total Li loaded onto the column was considered negligible. All collections are dried at 120 °C and then redissolved in 2 vol. % HNO_3.

The Li isotopic ratios of samples are determined by a double focusing multi-collector ICP–MS (MC–ICP–MS) at the IGCAS. The sample Li concentrations are measured by comparing signal intensities of sample solution with a 50 ppb IRMM-016 standard solution and adjusting sample concentration by using 2% vol. HNO_3 to obtain 50 ppb Li solutions. High-sensitive (X) cones are used to obtain about 1.2 V/50 ppb signals, and three blocks of 20 cycles are set up for each measurement. The δ^7Li value of each sample is effectively corrected by the standard sample (IRMM-016) bracketing method (SSB). The data are reported in standard δ-notation in per mil (‰) relative to IRMM-016 Li standard:

$$\delta^7 Li = \left[\left({}^7Li/{}^6Li \right)_{sample} / \left({}^7Li/{}^6Li \right)_{Irmm-016} - 1 \right] \times 1000(‰) \quad (1)$$

The long-term reproducibility for δ^7Li ratio measurement is ± 0.5‰ (2SD) (Xu et al. 2020). Two δ^7Li values of + 30.7 ± 0.2‰ (2SD) and + 30.8 ± 0.2‰ (2SD) are obtained for the seawater standard CASS-5 in this study (ESM2 Table S3), identical with the published δ^7Li values from + 30.4 to + 30.9‰ (Xu et al. 2020; Kil 2010).

Oxygen isotopes

The oxygen isotopes were measured by using a stable isotope ratio mass spectrometer (Thermo MAT-253) at the IGCAS. Quartz is ground to 200 mesh and analyzed using the BrF_5 method (Clayton and Mayeda 1963; Hou et al. 2015). The quartz reacted with BrF_5 to produce O_2, and then, O_2 reacted with kryptol converted into CO_2, which is collected in a sample tube. The O isotope compositions are reported in the δ-notation as the per mil (‰) deviation relative to the Vienna Standard Mean Ocean Water (V-SMOW), and the measurement precisions are ± 0.2‰.

Results

Vein type and quartz type classification

The quartz veins are classified into three types in terms of the ore-forming stages, including (i) the early quartz veins (QI) that are crosscut by stage II pyrite veins (Fig. 4a–c) where the quartz consists of an irregular CL-bright homogeneous quartz (QI_1; Fig. 5a) that is crosscut by thin vein-lets of a CL-dark homogeneous quartz (QI_2); (ii) the stage II quartz veins (QII) intergrown with arsenic-bearing pyrite and arsenopyrite (Fig. 4d–f) where the quartz consists of irregular CL-bright homogeneous cores (QII_1; Fig. 5f) overgrown by CL-dark irregular zoned rims (QII_2); and (iii) the stage III quartz veins (QIII) crosscutting the stage II pyrite assemblage (Fig. 4g–i) which also have a CL-bright zoned euhedral quartz ($QIII_1$) and dull-CL homogeneous quartz ($QIII_2$; Fig. 5m).

Fluid inclusion petrography and microthermometry

Fluid inclusions in different stages of quartz veins in the Shuiyindong gold deposit are dominantly by two-phase liquid-rich FIs with relatively small vapor bubbles (10–40 vol.% vapor) and vapor-rich FIs with a vapor volume of 55–99 vol.% (V-type; Fig. 5c, d). The two-phase liquid-rich FIs include the aqueous FIs (L-type) and aqueous-carbonic FIs (C-type). In addition, three-phase CO_2-rich FIs are scarce (C-type; Fig. 5k). Fluid inclusions trapped in quartz generally range from 10 to 30 μm in size, with only small amounts exceeding 30 μm, which always have negative crystal shape or rounded shape. The FIs presented in individual quartz grains but displayed in internal trails and three-dimensional groups are interpreted as pseudosecondary FIs (Fig. 5i), and the trails in crosscutting quartz grain boundaries are similarly interpreted as secondary FIs (Fig. 5n; Sterner and Bodnar 1984; Wilkinson 2001). During microthermometric measurements focused on primary and pseudosecondary FIs, only the L-type and C-type FIs were measured. We chose the samples with little secondary FIs, enriched in liquid-rich FIs and homogeneous populations of FIs for isotopic analysis. The eutectic temperatures of aqueous inclusions are difficult to observe, and only a few FIs show initial melting at about − 22 °C, implying predominance of NaCl in the FIs (Williams-Jones and Palmer 2002). The CO_2 melting temperatures in aqueous-carbonic inclusions range between − 59.8 and − 56.6 °C, mostly close to the Q3 point in the aqueous-carbonic system, suggesting predominance of CO_2 in volatiles (Wilkinson 2001). The thermometric results of all FIs in the Shuiyindong deposit are presented in ESM2 Table S2.

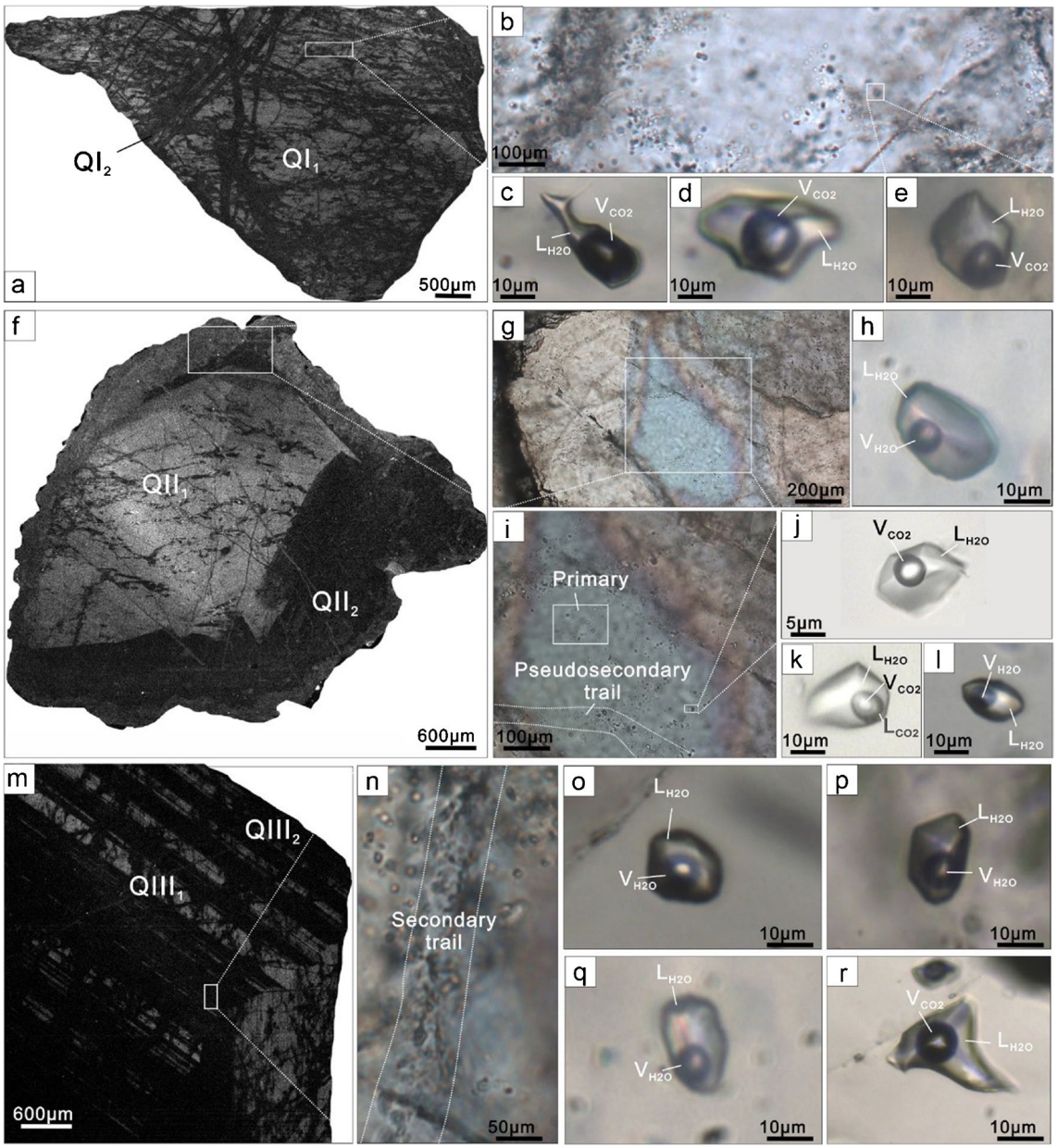

Fig. 5 **a** Irregular CL-bright quartz QI_1 crosscut by thin vein-lets of CL-dark QI_2 in stage I quartz veins. **b–e** QI veins with small-sized, two-phase aqueous-carbonic FIs. **d** Irregular CL-bright homogeneous cores (QII_1) overgrown by CL-dark irregular zoned rims (QII_2). **g–h** QII veins with small-sized, two-phase aqueous and aqueous-carbonic FIs. **i** QII veins with primary and pseudosecondary trail FIs. **j** Two-phase aqueous-carbonic FIs in the QII veins. **k** Three-phase carbonic FIs in the QII veins. **l** Two-phase aqueous FIs in the QII veins. **m** SEM-CL image of euhedral quartz in the QIII vein. **n** Secondary FIs in QIII vein. **o-q** Two-phase aqueous-carbonic FIs in QIII vein. **r** Two-phase aqueous-carbonic FIs in QIII vein

In stage I quartz (QI_1 and QI_2), primary L-type FIs have homogenization temperatures (Th) of 235 to 343 °C (LV→L; Fig. 6), ice melting temperatures from − 3.8 to − 1.3 °C, and salinities ranging from 4.5 to 6.2 wt% NaCl equiv (ESM1 Fig. S1). C-type FIs homogenize to liquid phase at temperatures of 251 to 325 °C (Fig. 5e). The melting of CO_2 clathrate (Tm_{clath}) occurred between 6.7 and 7.9 °C, with the calculated salinities of the aqueous phase ranging from 4.1 to 6.3 wt% NaCl equiv. The carbonic phases in C-type FIs homogenize into liquid phase at 19.7 to 26.7 °C.

In stage II quartz (QII_1 and QII_2), L-type FIs (Fig. 5h) have homogenization temperatures of 188 to 250 °C (LV→L), ice melting temperatures from − 3.1 to − 1.6 °C, and salinities ranging from 2.7 to 4.8 wt% NaCl equiv. C-type FIs (Fig. 5j–i) have Tm_{clath} from 7.6 to 8.8 °C, and the carbonic phases homogenize into liquid between 24.0 to 29.8 °C, salinities

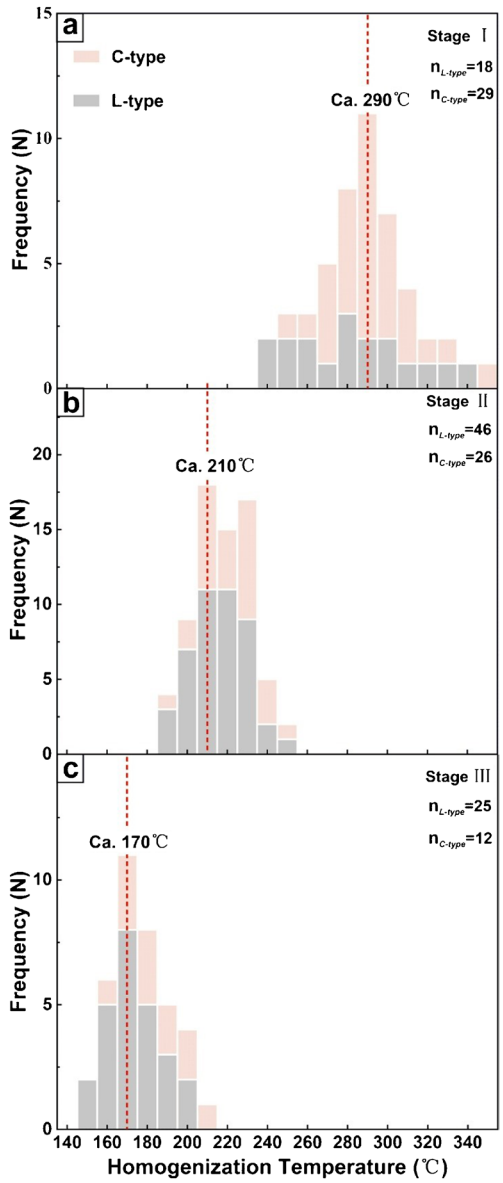

Fig. 6 Histograms of homogenization temperatures of fluid inclusions from different stages in the Shuiyindong gold deposit

ranging from 2.4 to 4.7 wt% NaCl equiv. They homogenized to liquid at temperatures of 189 to 250 °C.

In stage III quartz ($QIII_1$ and $QIII_2$), L-type FIs (Fig. 5o–p) homogenized to the liquid phase at temperatures of 154 to 204 °C. The ice melting temperatures range from − 2.0 to − 0.6 °C, with salinities values of 1.1 to 3.4 wt% NaCl equiv. C-type FIs (Fig. 5r) have homogenization temperature values of 162 to 211 °C (LV → L), Tm_{clath} from 8.7 to 9.6 °C, with salinities ranging from 0.8 to 2.6 wt% NaCl equiv. The carbonic phases homogenize between 27.2 and 31.2 °C, with homogenization into the liquid.

Lithium concentrations and isotopic compositions

Lithium concentrations of quartz from the Shuiyindong deposit range from 1.53 to 7.95 ppm and Li concentrations of quartz-hosted fluid inclusion leachates range from 12.3 to 66.8 ppb (ESM2 Table S3). The Li concentrations in FIs are calculated based on Cl and Li concentrations in leachates and salinity of each sample which derive from this fluid inclusion microthermometry study, using the estimated equation as follows (Teng et al. 2006b):

$$C_{Li(FIs)} = C_{Li(Leachates)} \times \left(C_{Cl(salinity)}/C_{Cl(Leachates)}\right) \quad (2)$$

The Cl concentrations in leachates were measured through ion chromatography. The stage I FIs have relatively high Li concentrations of 505 to 2733 ppm with an average of 1426 ppm. The stage II FIs vary from 136 to 854 ppm, with an average of 332 ppm. The calculated Li concentrations of stage III FIs are 63 to 144 ppm, with an average of 95 ppm.

Li isotopes of the different stages of quartz-hosted fluid inclusion are summarized in ESM2 Table S3. The measured δ^7Li values of the three stages vary broadly from + 5.1 to + 22.8‰ ($n = 37$) and show systematic variations with different stages. The stage I FIs have δ^7Li values ranging from + 5.1 to + 9.0‰, with an average of + 7.3 ± 0.4‰ ($n = 11$). The stage II FIs have δ^7Li values ranging from + 9.3 to + 16.1‰, with an average of + 13.0 ± 0.4‰ ($n = 17$). The stage III δ^7Li values of FIs are prominently heavier with δ^7Li of + 15.5 to + 22.8‰, averaging + 17.8 ± 0.7‰ ($n = 9$).

O isotope compositions

The δ^{18}O values of quartz vary from + 8.0 to + 18.0‰ (ESM2 Table S3). The $\delta^{18}O_{quartz}$ values of stage I range from + 14.0 to + 17.4‰ ($n = 5$). The $\delta^{18}O_{quartz}$ values of stage II range from + 11.4 to + 18.0‰ ($n = 5$). The stage III $\delta^{18}O_{quartz}$ range from + 8.1 to + 11.1‰ ($n = 4$). The calculated δ^{18}O values of the ore-forming fluids use the equilibrium fractionation equation of quartz–water as follows (Zheng 1993):

$$\delta^{18}O_{fluid} = \delta^{18}O_{quartz} - (4.48 \times 10^6/T^2 - 4.77 \times 10^3/T + 1.71) \quad (3)$$

The $\delta^{18}O_{fluid}$ values are calculated with the average temperature obtained by microthermometric studies of each sample. The $\delta^{18}O_{fluid}$ values of stage I are from + 6.3 to + 10.0‰ (average of + 8.6‰; $n = 5$). The $\delta^{18}O_{fluid}$ values of stage II range from + 0.1 to + 7.7‰ with an average of + 3.8‰ ($n = 5$). The stage III $\delta^{18}O_{fluid}$ values range from − 5.4 to − 2.8‰ (average of − 3.9‰; $n = 4$).

Discussion

Characteristics and nature of ore-forming fluids

The quartz-hosted FIs analyzed in this study are characterized by relatively low salinity and temperature (salinities of 0.8 to 6.3 wt% NaCl equiv and Th values of 154 to 343 °C, Fig. 6; ESM1 Fig. S1). The early fluids at the Shuiyindong are recorded by the stage I FIs which have Th values of 235 to 343 °C, salinity values ~ 5 wt% NaCl equiv, and are CO_2-rich. Stage II FIs have salinities of ~ 4 wt% NaCl equiv, whereas Th decreased to 210 ~ 230 °C. The stage III fluids have Th values of ~ 170 °C, with low salinities of ~ 2.5 wt% NaCl equiv. As outlined above, the Th and salinities of fluid inclusions generally decrease from early to late stages. Notably, the stage II fluids show an obvious positive correlation between salinity and Th (Fig. 7). Mixing between two fluids is suggested by the correlation between homogenization temperatures and salinity of aqueous and aqueous-carbonic inclusions (Ruggieri et al. 1999; Wilkinson 2001), where the change of salinities is likely attributed to the aqueous fluids tending to decrease as fluid mixing proceeded. This interpretation is supported by noble gas date (He–Ne-Ar) that revealed mixed signatures of initial magmatic fluids and external fluids (Jin et al. 2020). Collectively, the mixing processes may provide the crucial conditions for effective precipitation of gold and other sulfides during mineralization at the Shuiyindong gold deposit.

Li–O isotopic constraints on fluid mixing

The ore-forming fluids of the Shuiyindong deposit have considerably variable δ^7Li and δ^{18}O values (δ^7Li values from + 5.1 to + 22.8‰; δ^{18}O values from − 5.4 to + 10.0‰, ESM2 Table S3). A gradual enrichment of heavy Li isotopes and light O isotopes is observed from the stage I to stage III. For example, the stage II fluids are characterized by heavier Li (+ 9.3 to + 16.1‰, with an average of + 13‰; Fig. 8a), but lighter O isotopic compositions relative to the stage I (+ 0.1 to + 7.7‰, with an average of + 3.8‰). The microthermometric studies of stage II show mixed signatures of different end-members. Furthermore, Fig. 9a shows Li/Cl ratios that are negatively correlated with the δ^7Li values, and the negative correlation could be best explained by fluid mixing that involves a low δ^7Li value fluid and a higher δ^7Li value fluid with low Li/Cl ratio. Thus, the positive shift of Li isotopes can be ascribed to mixing of external heavier isotope reservoirs. A similar case was observed in the Carlin gold deposits in the Jerritt Canyon district, Nevada, where gold deposition was a consequence

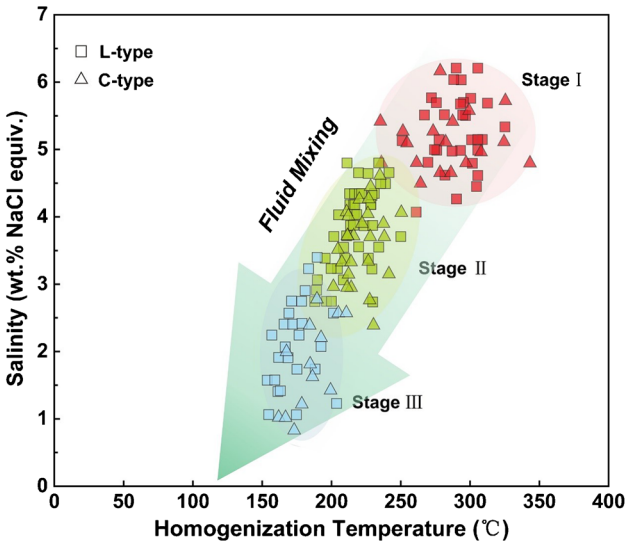

Fig. 7 Homogenization temperatures versus salinities of fluid inclusions from different stages in the Shuiyindong gold deposit. The red box represents L-type fluid inclusions of stage I, and red triangle represents C-type fluid inclusions of stage I. The green box represents L-type fluid inclusions of stage II, and green triangle represents C-type fluid inclusions of stage II. The blue box represents L-type fluid inclusions of stage III, and blue triangle represents C-type fluid inclusions of stage III

of fluid mixing (Hofstra et al. 1991). The calculated δ^{18}O values of fluids in equilibrium with quartz from stage II have a slightly heavier δ^{18}O signature with a maximum at + 7.7‰, and the minimum $\delta^{18}O_{fluid}$ of + 0.1‰ for the fluids may represent fluid mixing between ^{18}O-enriched source and ^{18}O-depleted reservoir. The mixed fluids will inherit the characteristics of heavy oxygen isotopes when ^{18}O-enriched fluids account for a large fraction of fluid mixing, such as a value of 7.7‰ is coherent with the oxygen isotope composition of the magmatic fluid. Thus, the stage II fluids likely resulted from the mixing of two fluids.

Constraints on fluid sources and evolution by Li–O isotopes

The stage I fluids have higher δ^7Li values (+ 5.1 to + 9.1‰) compared to granitic melts (− 5 to + 5‰) constrained by previous studies (Pogge von Strandmann et al. 2011; Masukawa et al. 2013; Richard et al. 2018; Xu et al. 2018, 2021). Masukawa et al. (2013) studied a magmatic-hydrothermal W-Sn deposit and observed light Li isotopic compositions (− 1.4 to + 10.1‰) of FIs trapped in quartz. Yang et al. (2015) found similar isotopic fractionation between FIs (+ 4.5‰) and andesite (+ 1 to + 2‰) related to mineralization, supporting a magmatic origin for a VMS Pb–Zn deposit. The preferential partitioning

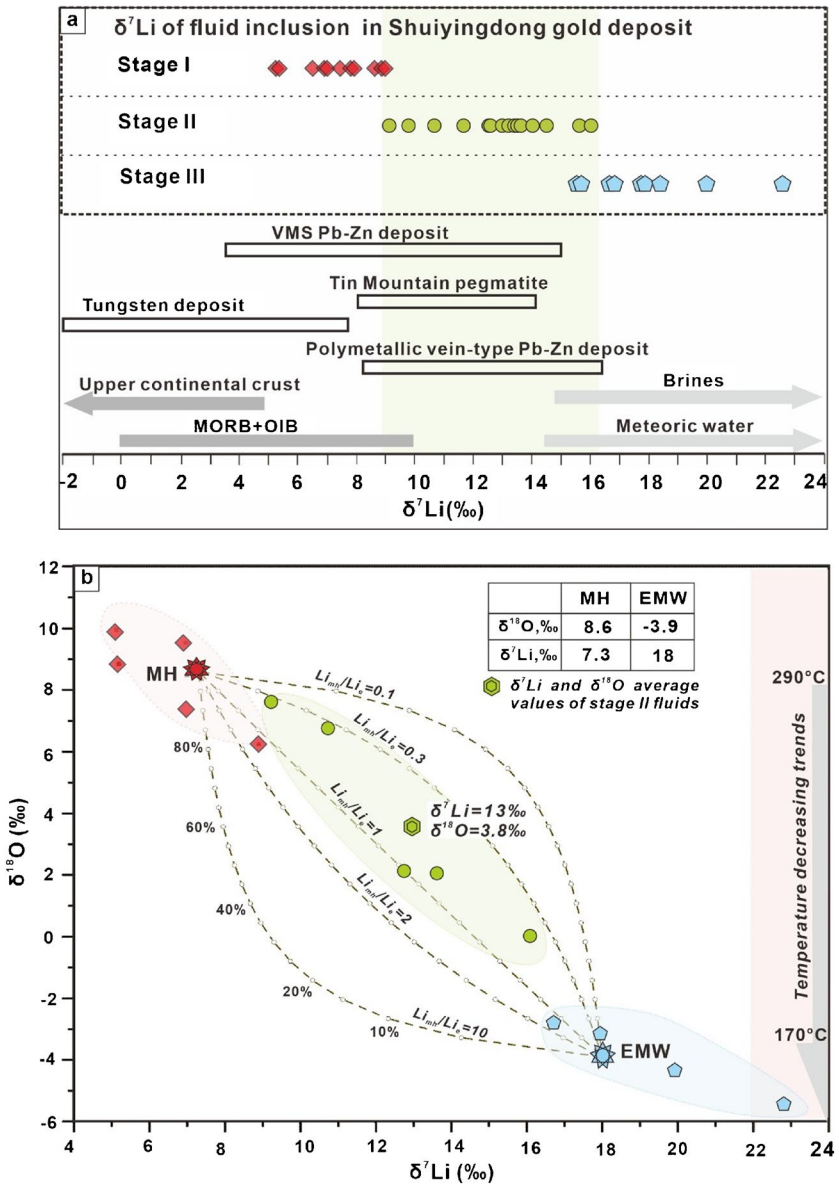

Fig. 8 **a** Ranges of Li isotope compositions of fluid inclusions from different stage in the Shuiyindong gold deposit. The lower boxes show δ^7Li date from other deposits and the δ^7Li ranges of natural Li reservoirs (Teng et al. 2004, 2006a, b; Sauzeat et al. 2015 and references therein). **b** Diagram showing mixing model of Li–O isotopic compositions of stage II fluids. The δ^7Li and δ^{18}O values of the magmatic-hydrothermal fluids (MH) and the exchanged meteoric water (EMW) are averages of stage I and stage III fluids, respectively (see text for details). Brown lines represent different ratios of Li concentrations in magmatic-hydrothermal fluids (Li_{mh}) and exchanged meteoric water (Li_e). Percentage represents mole fractions of magmatic-hydrothermal fluids in the fluid system. Gray arrow shows trend of temperatures

of Li into aqueous fluids over granitic melts at the condition of equilibrium is accompanied with small Li isotope fractionation (< 4‰) (Webster et al. 1989). Teng et al. (2006b) conducted research on the S-type Harney Peak granite and associated Tin Mountain pegmatite and proposed that the δ^7Li values of magmatic fluids were approximately 4‰ higher than in the parental magma. The above observations may indicate that the δ^7Li values of stage I fluids are in accordance with the Li-isotopic range of magmatic fluids (about − 1 to + 9‰). Additionally, the calculated δ^{18}O values of fluids in stage I (+ 6.3 to + 10.0‰, with an average of + 8.6‰) are in accordance with the reported magmatic O-isotopic range (+ 5.3 to + 10.0‰) and indicate a dominantly magmatic fluid source. This interpretation is also supported by previous H–O and S isotope data which record the footprint of magmatic fluids at the Shuiyindong gold deposit (Tan et al. 2015a; Xie et al. 2018). Combined with previous stable isotopic evidence, the Li–O isotopic signatures of stage I ore-forming fluids reflect a magmatic-hydrothermal source.

The stage III fluids have δ^7Li and δ^{18}O values from + 15.5 to + 22.8‰ (avg. + 18.0‰) and − 5.4 to − 2.8‰ (avg. − 3.9‰; Fig. 8a), respectively. Moreover, the Li concentrations of stage III fluids (63 to 144 ppm) are significantly lower than stage I and stage II fluids (136 to 2733 ppm), and this discrepancy suggests that the stage III fluids are unlikely of the same

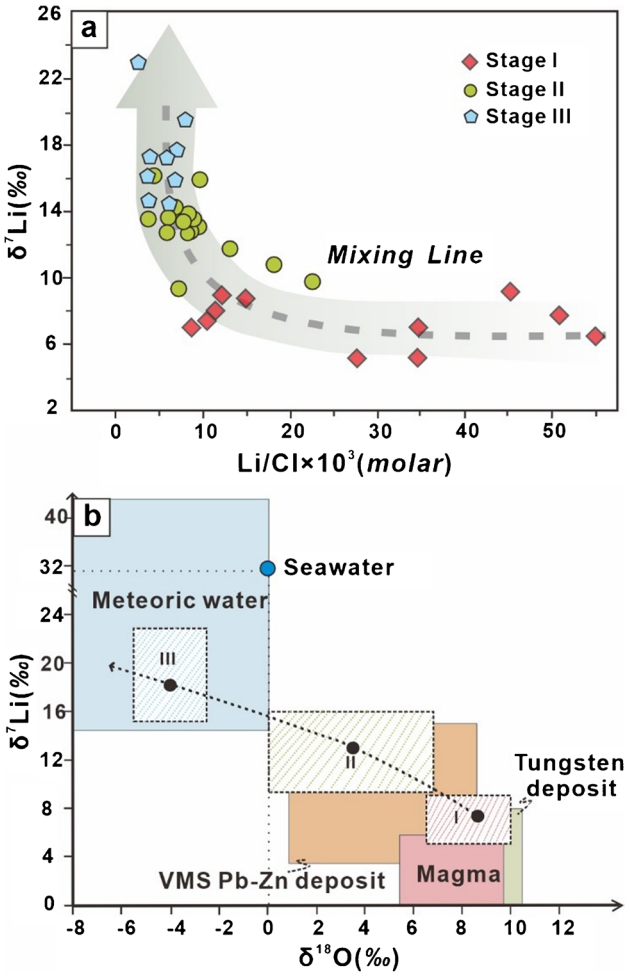

Fig. 9 **a** Correlation between δ^7Li values and Li/Cl ratios. **b** Combined Li–O isotopic variations of fluids in different stages from Shuiyindong. Data for Li isotopes of the reservoirs are the same as those in Fig. 8a, while oxygen isotope ranges of these reservoirs are from Taylor (1974). Oxygen isotope range of a tungsten deposit and a VMS Pb–Zn deposit are from Shibue et al. (2005) and Yang et al. (2015), respectively

origin as the stage I and stage II fluids. The δ^{18}O signatures indicate ^{18}O-depleted basinal brines or meteoric water (Taylor 1974; Schwinn et al. 2006). Bottomley et al. (1999) reported that the Canadian Shield brines reach total salinities of more than 10 wt% NaCl equiv, which have Li isotope compositions of + 14.8 to + 44.8‰. However, in our study, microthermometric dates show that the ore-forming fluids have extremely low salinities (0.8–3.4 wt% NaCl equiv.) far below the basinal brine salinity, so it is very unlikely that the stage III fluids relate to basinal brines. Millot et al. (2010a) and Pogge von Strandmann et al. (2010) found that the Li isotopic composition of meteoric water from France and Sao Miguel is distinctively heavy (> + 21.9‰) with extremely low Li concentrations (< 10 ppb). The Li concentrations of stage III fluids are significantly higher than in meteoric water and may be attributed to water–rock interaction that can cause distinctively heavy Li isotopic composition and loss of Li from the sedimentary rocks into the fluids (Chan et al. 1994; Meredith et al. 2013; Millot et al. 2010b; Pogge von Strandmann et al. 2014). Assuming a water/rock ratio of 0.5 and average rock density of 2600 kg/m^3, the Li concentration of exchanged fluids calculated by the exchange model between the sediments and meteoric water (Li = 0.01 ppm) is 80, 160, and 240 ppm, corresponding the initial Li concentration of sedimentary rocks in Shuiyindong deposit of 50, 100, and 150 ppm Li (Tan et al. 2015b). The model suggests that the exchange processes will add Li from the host rocks to the fluids (ESM1 Fig. S2; ESM2 Table S4). Therefore, fluids of meteoric origin, which are exchanged with sedimentary rocks (exchanged meteoric water), can exhibit increasing Li concentration compared to the initial meteoric water. Collectively, the combination of higher Li and lower O isotopic signatures of stage III fluids thus can be coherently explained by meteoric water that has interacted with sedimentary rocks.

Modeling of the Li and O isotope composition of mixed fluids

Based on the above discussion, a fluid mixing model is presented to elucidate the ore-forming process. Fluid mixing can cause significant changes in physico-chemical properties such as temperature and Li–O isotopic composition. In this study, the abrupt drop in temperature (from 343 to 154 °C), combined with the increasing δ^7Li values (from + 5.1 to + 22.8‰) and decreasing δ^{18}O values (from + 10 to − 5.4‰), indicates that the magmatic fluid source is waning over time and more meteoric water is entering the system. In particular, the drastic changes in stage II fluids may have resulted from fluid mixing between magmatic fluids and meteoric water. Similar processes have been well documented in porphyry and skarn systems (Cook et al. 2011; Shu et al. 2020). To provide quantitively constraints on this mixing process, we assume that the stage I fluids are representative of the end-member of magmatic fluids with the δ^7Li of + 7.3‰ and δ^{18}O values of + 8.6‰ (calculated by average δ^7Li and δ^{18}O values of all samples in stage I) and the stage III fluids are representative of the end-member of exchanged meteoric water with δ^7Li of + 18‰ and δ^{18}O values of − 4‰ (average δ^7Li and δ^{18}O values of all samples in stage III). Modeling of the mixing process between meteoric water and magmatic fluids is complicated due to the uncertainties of Li concentrations in end-members

and the inevitable Li uptake within quartz. The different ratios of Li contents of meteoric water (Li_e) and magmatic-hydrothermal fluids (Li_{mh}) are adopted for characterizing the binary mixing processes (ESM1 and ESM2 Table S5). The mixing equations for lithium and oxygen isotopes based on isotopic mass balance can be expressed as (Schwinn et al. 2006):

$$\delta^7Li_M = \frac{m_{mh(Li)}f_{mh}}{m_{mh(Li)}f_{mh} + m_{e(Li)}(1-f_{mh})} \times \delta^7Li_{mh} + \frac{m_{e(Li)}(1-f_{mh})}{m_{mh(Li)}f_{mh} + m_{e(Li)}(1-f_{mh})} \times \delta^7Li_e \quad (4)$$

$$\delta^{18}O_M = \frac{m_{mh(O)}f_{mh}}{m_{mh(O)}f_{mh} + m_{e(O)}(1-f_{mh})} \times \delta^{18}O_{mh} + \frac{m_{e(O)}(1-f_{mh})}{m_{mh(O)}f_{mh} + m_{e(O)}(1-f_{mh})} \times \delta^{18}O_e \quad (5)$$

The δ^7Li_{mh}, δ^7Li_e, and δ^7Li_M values represent the Li isotope compositions for the magmatic-hydrothermal fluids, the meteoric water, and the mixture, respectively. The $\delta^{18}O_{mh}$, $\delta^{18}O_e$, and $\delta^{18}O_M$ values represent the O isotope composition for the magmatic-hydrothermal fluids, the meteoric water, and the mixture, respectively. f_{mh} denotes the mole fractions of magmatic-hydrothermal fluids in the mixture; $m_{mh(Li)}$ and $m_{e(Li)}$ are the molarities of Li in the magmatic-hydrothermal fluids and meteoric water, respectively. As shown in Fig. 8b, the stage II fluids with low Li_{mh}/Li_e ratios from 1 to 0.3 may be attributed to exchanged meteoric water. The gradually decreasing contribution of the magmatic component suggests that the ore-forming fluids evolve from magmatic fluids to meteoric waters over time. This model indicates that both the magmatic fluids and exchanged meteoric waters in stage II fluids are favorable for ore mineralization.

In summary, the observation of the systematic Li–O isotopic changes of the ore-forming fluids can be attributed to mixing between magmatic fluids and meteoric water (Fig. 9b). The fluid mixing process modified the physical and chemical conditions of the ore-forming fluids and caused the Li–O isotopic variations observed in fluids inclusion trapped in quartz of different stages at the Shuiyindong gold deposit (Fig. 10).

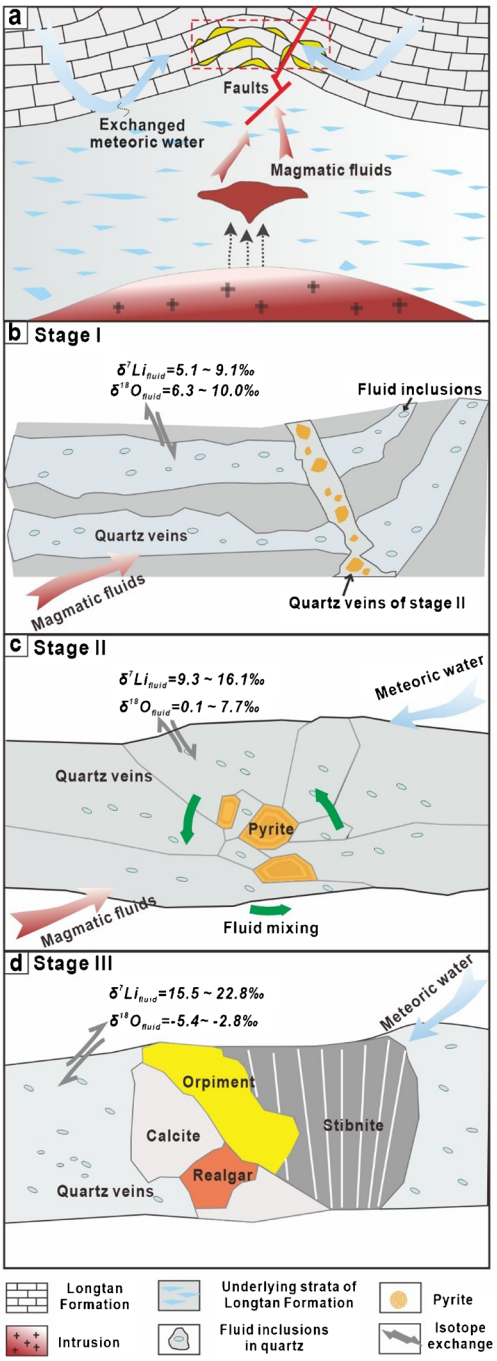

Fig. 10 Diagram showing the hydrothermal evolution of the Shuiyindong deposit. **a** Model for mixing between magmatic fluid and exchanged meteoric water. **b–d** Paragenetic relationships of quartz and pyrite, entrapment of fluid inclusions, fluid evolution through time, and Li–O isotopic compositions of the fluids

Conclusions

Geochemical signatures of three stages of FIs hosted in quartz provide new insights into the source and evolution of ore-forming fluids in the giant Shuiyindong Carlin-type gold deposit in SW China. The FIs microthermometry data suggest that the ore-forming fluids are characterized by low salinity (0.8–6.3 wt% NaCl equiv.) and moderate temperature (154–343 °C). Combined Li–O isotope compositions of fluid inclusions are suggestive of two end-member mixing of magmatic and meteoric components. This mixing is considered as an important process to trigger gold mineralization.

Our study highlights that the combined use of Li and O isotopes is a powerful tool to constrain the source and evolution of complex hydrothermal mineralizing systems.

Supplementary Information The online version contains supplementary material available at https://doi.org/10.1007/s00126-023-01211-w.

Acknowledgements We would like to thank Mr. Ting Zhou and Ms. Min Wang for helping with Li isotope analyses, to Mr. Jiayi Feng for helping with O isotope analyses, and to Ms. Jiali Cai for assistance in fluid inclusion observation. We appreciate the constructive comments and suggestions of Patrick Carr, Matthieu Harlaux, and an anonymous reviewer, which significantly improved the quality of data interpretation of the manuscript. We are grateful to Yang Li (Associate Editor) and Bernd Lehmann (Editor-in-Chief) for their constructive comments and promoting handling of the manuscript.

Funding This research was financially supported by the National Natural Science Foundation of China (41830432, U1812402).

Declarations

Conflict of interest The authors declare no competing interests.

References

Bodnar RJ (1993) Revised equation and table for determining the freezing point depression of H_2O-NaCl solutions. Geochim Cosmochim Acta 57:683–684

Bottomley D, Katz A, Chan LH, Starinsky A, Douglas M, Clark ID, Raven KG (1999) The origin and evolution of Canadian Shield brines: evaporation or freezing of seawater? New lithium isotope and geochemical evidence from the Slave craton. Chem Geol 155:295–320

Bottomley D, Chan L, Katz A, Starinsky A, Clark I (2003) Lithium isotope geochemistry and origin of Canadian Shield brines. Groundwater 41:847–856

Brant C, Coogan LA, Gillis KM, Seyfried WE, Pester NJ, Spence J (2012) Lithium and Li-isotopes in young altered upper oceanic crust from the East Pacific Rise. Geochim Cosmochim Acta 96:272–293

Cai JX, Zhang KJ (2009) A new model for the Indochina and South China collision during the late Permian to the Middle Triassic. Tectonophysics 467:35–43

Chan LH, Gieskes JM, You CF, Edmond JM (1994) Lithium isotope geochemistry of sediments and hydrothermal fluids of the Guaymas Basin, Gulf of California. Geochim Cosmochim Acta 58:4443–4454

Chan LH, Starinsky A, Katz A (2002) The behavior of lithium and its isotopes in oilfield brines: evidence from the Heletz-Kokhav field, Israel. Geochim Cosmochim Acta 66:615–623

Chen MH, Lu G, Li XH (2012) Muscovite $^{40}Ar/^{39}Ar$ dating of the quartz porphyry veins from northwest Guangxi, China, and its geological significance. Geol J China Univ 18:106–116 (in Chinese with English abs.)

Cheng YB, Mao JW, Xie GQ, Chen MH, Yang ZX (2009) Zircon U-Pb dating of granite in Gejiu super-large tin polymetallic orefield and its significance. Mineral Deposits 28:297–312 (in Chinese with English abs.)

Cheng YB, Mao JW, Chen XL, Li W (2010) LA-ICP-MS zircon U-Pb dating of the Bozhushan granite in southeastern Yunnan Province and its significance. J Jilin Univ (Earth Sci Edn) 40:869–878 (in Chinese with English abs.)

Clayton RN, Mayeda TK (1963) The use of bromine pentafluoride in the extraction of oxygen from oxides and silicates for isotopic analysis. Geochim Cosmochim Acta 27:43–52

Cline JS, Hofstra AH, Muntean JL, Tosdal RM, Hickey KA (2005) Carlin-type gold deposits in Nevada: Critical geologic characteristics and viablemodels. In: Hedenquist JW et al. (eds) Economic Geology 100th Anniversary Volume, Soc Econ Geol, pp 451–484

Cook DR, Deyell CL, Waters PJ, Gonzales RI, Zaw K (2011) Evidence for magmatic-hydrothermal fluids and ore-forming processes in epithermal and porphyry deposits of the Baguio district, Philippines. Econ Geol 106(8):1399–1424

Deveaud S, Millot R, Villaros A (2015) The genesis of LCT-type granitic pegmatites, as illustrated by lithium isotopes in micas. Chem Geol 411:97–111

Du YS, Huang HW, Huang ZQ, Xu YJ, Yang JH, Huang H (2009) Basin translation from late Paleozoic to Triassic of Youjiang basin and its tectonic signification. Geol Sci Technol Inf 28:10–15 (in Chinese with English abs.)

Du YS, Huang H, Yang JH, Huang HW, Tao P, Huang ZQ, Hu LS, Xie CX (2013) The basin translation from late Paleozoic to Triassic of the Youjiang basin and its tectonic signification. Geol Rev 59:1–11 (in Chinese with English abs.)

Emsbo P, Hofstra AH, Lauha EA, Griffin GL, Hutchinson RW (2003) Origin of high-grade gold ore, source of ore fluid components, and genesis of the Meikle and neighboring Carlin-type deposits, northern Carlin trend, Nevada. Econ Geol 98:1069–1105

Feng JR, Mao JW, Pei RF, Zhou ZH, Yang ZX (2010) SHRIMP zircon U-Pb dating and geochemical characteristics of Laojunshan granite intrusion from the Wazha tungsten deposit, Yunnan Province and their implications for petrogenesis. Acta Petrol Sin 26:845–857 (in Chinese with English abs.)

Fusswinkel T, Wagner T, Walle M, Wenzel T, Heinrich CA, Mark LG (2013) Fluid mixing forms basement-hosted Pb-Zn deposits: insight from metal and halogen geochemistry of individual fluid inclusions. Geology 41:679–682

Gao W, Hu RZ, Hofstra AH, Li QL, Zhu JJ, Peng KQ, Mu L, Huang Y, Ma JW, Zhao Q (2021) U-Pb dating on hydrothermal rutile and monazite from the Badu gold deposit supports an Early Cretaceous age for Carlin-type gold mineralization in the Youjiang Basin, southwestern China. Econ Geol 116:1355–1385

Gao W, Hu RZ, Mei L, Bi XW, Fu SL, Huang ML (2022) Monitoring the evolution of sulfur isotope and metal concentrations across gold-bearing pyrite of Carlin-type gold deposits in the Youjiang Basin, SW China. Ore Geol Rev 147:104990

Halama R, Savov IP, Rudnick RL, McDonough WF (2009) Insights into Li and Li isotope cycling and sub-arc metasomatism from veined mantle xenoliths, Kamchatka. Contrib Mineral Petrol 158:197–222

Harlaux M, Kouzmanov K, Gialli S, Marger K, Bouvier AS, Baumgartner LP, Rielli A, Dini A, Chauvet A, Kalinaj M, Fontboté L (2021) Fluid mixing as primary trigger for cassiterite deposition: evidence from in situ $\delta^{18}O$-$\delta^{11}B$ analysis of tourmaline from the world-class San Rafael tin (-copper) deposit, Peru. Earth Planet Sci Lett 563:116889

Hedenquist JW, Lowenstern JB (1994) The role of magmas in the formation of hydrothermal ore deposits. Nature 370:519–527

Hofstra AH, Leventhal JS, Northrop HR, Landis GP, Rye RO, Birak DJ, Dahl AR (1991) Genesis of sediment-hosted disseminated gold deposits by fluid mixing and sulfidization: chemical-reaction-path modeling of ore-depositional processes documented in the Jerritt Canyon district, Nevada. Geology 19:36–40

Hou ZQ, Khin Z, Qu XM, Ye QT, Yu JJ, Xu MJ, Fu DM, Yin XK (2001) Origin of the gacun volcanic-hosted massive sulfide deposit in Sichuan, China: fluid inclusion and oxygen isotope evidence. Econ Geol 96:1491–1512

Hou ZQ, Liu Y, Yang ZM, Tian SH, Xie YL (2015) Formation of carbonatite-related giant rare-earth-element deposits by the recycling of marine sediments. Sci Rep 5:1023

Hou L, Peng HJ, Ding J, Zhang JR, Zhu SB, Wu SY, Wu Y, Ouyang HG (2016) Textures and in situ chemical and isotopic analyses of pyrite, Huijiabao trend, Youjiang basin, China: Implications for paragenesis and source of sulfur. Econ Geol 111:331–353

Hu RZ, Su WC, Bi XW, Tu GZ, Hofstra AH (2002) Geology and geochemistry of Carlin-type gold deposits in China. Miner Deposita 37:378–392

Hu RZ, Fu SL, Huang Y, Zhou MF, Fu SH, Zhao CS, Wang YJ, Bi XW, Xiao JF (2017) The giant South China Mesozoic low-temperature metallogenic domain: reviews and a new geodynamic model. J Asian Earth Sci 137:9–34

James RH, Palmer MR (2000) The lithium isotope composition of international rock standards. Chem Geol 166:319–326

James RH, Allen DE, Seyfried WE (2003) An experimental study of alteration of oceanic crust and terrigenous sediments at moderate temperatures (51 to 350 °C): insights as to chemical processes in near-shore ridge-flank hydrothermal systems. Geochim Cosmochim Acta 67:681–691

Jin XY, Hofstra AH, Hunt AG, Liu JZ, Yang W, Li JW (2020) Noble gases fingerprint the source and evolution of ore-forming fluids of carlin-type gold deposits in the golden triangle, South China. Econ Geol 115:455–469

Jin XY, Zhao JX, Feng YX, Hofstra AH, Deng XD, Zhao XF, Li JW (2021) Calcite U-Pb dating unravels the age and hydrothermal history of the giant Shuiyindong Carlin-type gold deposit in the golden triangle, South China. Econ Geol 116:1253–1265

Kil Y (2010) Lithium isotopic disequilibrium of minerals in the spinel lherzolite xenoliths from Boeun, Korea. J Geochem Explor 107:56–62

Krienitz MS, Garbe-Schönberg CD, Romer RL, Meixner A, Haase KM, Stronick NA (2012) Lithium isotope variations in ocean island basalts-implications for the development of mantle heterogeneity. J Petrol 53:2333–2347

Large SJE, Bakker EYN, Weis P, Wälle M, Ressel M, Heinrich CA (2016) Trace elements in fluid inclusions of sediment-hosted gold deposits indicate a magmatic-hydrothermal origin of the Carlin ore trend. Geology 44:1015–1018

Li ZX, Li XH (2007) Formation of the 1300-km-wide intracontinental orogen and postorogenic magmatic province in Mesozoic South China: A flat-slab subduction model. Geology 35:179–182

Li JX, Hu RZ, Zhao CH, Zhu JJ, Huang Y, Gao W, Zhuo YZ (2020) Sulfur isotope and trace element compositions of pyrite determined by NanoSIMS and LA-ICP-MS: new constraints on the genesis of the Shuiyindong Carlin-like gold deposit in SW China. Miner Deposita 55:1279–1298

Li Y, Zhang RQ, He S, Chiaradia M, Li XH (2022) Pulsed exsolution of magmatic ore-forming fluids in tin-tungsten systems: a SIMS cassiterite oxygen isotope record. Miner Deposita 57:343–352

Liu S, Su WC, Hu RZ, Feng CX, Gao S, Coulson IM, Wang T, Feng GY, Tao Y, Xia Y (2010) Geochronological and geochemical constraints on the petrogenesis of alkaline ultramafic dykes from southwest Guizhou Province, SW China. Lithos 114:253–264

Masukawa K, Nishio Y, Hayashi KI (2013) Lithium-strontium isotope and heavy metal content of fluid inclusions and origin of ore-forming fluid responsible for tungsten mineralization at Takatori mine, Japan. Geochem J 47:309–319

Meredith K, Moriguti T, Tomascak P, Hollins S, Nakamura E (2013) The lithium, boron and strontium isotopic systematics of groundwaters from an arid aquifer system: implications for recharge and weathering processes. Geochim Cosmochim Acta 112:20–31

Millot R, Négrel P, Petelet-Giraud E (2007) Multi-isotopic (Li, B, Sr, Nd) approach for geothermal reservoir characterization in the Limagne Basin (Massif Central, France). Applied Geochem 22:2307–2325

Millot R, Petelet-Giraud E, Guerrot C, Négrel P (2010a) Multi-isotopic composition (δ^7Li–δ^{11}B–δD–δ^{18}O) of rainwater in France: origin and spatio-temporal characterization. Applied Geochem 25:1510–1524

Millot R, Vigier N, Gaillardet J (2010b) Behaviour of lithium and its isotopes during weathering in the Mackenzie Basin, Canada. Geochim Cosmochim Acta 74:3897–3912

Muntean JL, Cline JS, Simon AC, Longo AA (2011) Magmatic-hydrothermal origin of Nevada's Carlin-type gold deposits. Nature Geosci 4:122–127

Nishio Y, Nakai S, Yamamoto J, Sumiao H, Matsumoto T, Prikhod'ko VS, Arai S (2004) Lithium isotopic systematics of the mantle-derived ultramafic xenoliths: implications for EM1 origin. Earth Planet Sci Let 217:245–261

Peng YW, Gu XX, Zhang YM, Liu L, Wu CY, Chen SY (2014) Ore-forming process of the Huijiabao gold district, southwestern Guizhou Province, China: evidence from fluid inclusions and stable isotopes. J Asian Earth Sci 93:89–101

Pettke T, Oberli F, Heinrich CA (2010) The magma and metal source of giant porphyry-type ore deposits, based on lead isotope microanalysis of individual fluid inclusions. Earth Planet Sci Lett 296:267–277

Pi QH, Hu RZ, Xiong B, Li QL, Zhong RC (2017) In situ SIMS U-Pb dating of hydrothermal rutile, reliable age for the Zhesang Carlin-type gold deposit in the golden triangle region, SW China. Miner Deposita 52:1179–1190

Pogge von Strandmann PAE, Burton KW, James RH, van Calsteren P, Gislason SR (2010) Assessing the role of climate on uranium and lithium isotope behaviour in rivers draining a basaltic terrain. Che Geol 270:227–239

Pogge von Strandmann PAE, Elliott T, Marschall HR, Coath C, Lai YJ, Jeffcoate AB, Ionov DA (2011) Variations of Li and Mg isotope ratios in bulk chondrites and mantle xenoliths. Geochim Cosmochim Acta 75:5247–5268

Pogge von Strandmann PAE, Porcelli D, James RH, van Calsteren P, Schaefer B, Cartwright I, Reynolds BC, Burton KW (2014) Chemical weathering processes in the Great Artesian Basin: evidence from lithium and silicon isotopes. Earth Planet Sci Lett 406:24–36

Qiu L, Yan DP, Tang SL, Wang Q, Yang WX, Tang XL, Wang JB (2016) Mesozoic geology of southwestern China: Indosinian foreland overthrusting and subsequent deformation. J Asian Earth Sci 122:91–105

Richard A, Cathelineau M, Boiron MC, Mercadier J, Banks DA, Cuney M (2016) Metal-rich fluid inclusions provide new insights into unconformity-related U deposits (Athabasca Basin and Basemen, Canada). Mine Deposita 51:249–270

Richard A, David A, Banks DA, Hendrikssona N, Lahayea Y (2018) Lithium isotopes in fluid inclusions as tracers of crustal fluids: an exploratory study. J Geochem Explor 184:158–166

Ruggieri G, Cathelineau M, Boiron MC, Marignac C (1999) Boiling and fluid mixing in the chlorite zone of the Larderello geothermal system. Che Geol 154:237–256

Rusk BG, Reed MH, Dilles JH (2008) Fluid inclusion evidence for magmatic-hydrothermal fluid evolution in the porphyry copper-molybdenum deposit at Butte, Montana. Econ Geol 103:307–334

Ryan JG, Kyle PR (2004) Lithium abundance and lithium isotope variations in mantle sources: insights from intraplate volcanic rocks from Ross Island and Marie Byrd Land (Antarctica) and other oceanic islands. Chem Geol 212:125–142

Sauzeat L, Rudnick RL, Chauvel C, Garcon M, Tang M (2015) New perspectives on the Li isotopic composition of the upper continental crust and its weathering signature. Earth Planet Sci Lett 428:181–192

Schwinn G, Wagner T, Baatartsogt B, Markl G (2006) Quantification of mixing processes in ore-forming hydrothermal systems by combination of stable isotope and fluid inclusion analyses. Geochim Cosmochim Acta 70:965–982

Shibue Y, Chiba H, Kusakabe M (2005) temperatures and oxygen Isotopic composition on hydrothermal fluids for the Takatori tungsten-copper deposit, Japan. Resource Geo 55(2):101–110

Shu QH, Chang ZS, Mavrogenes J (2020) Fluid compositions reveal fluid nature, metal deposition mechanisms, and mineralization potential: an example at the Haobugao Zn-Pb skarn, China. Geology 49(4):473–477

Silliton RH, Bonham HF (1990) Sediment-hosted gold deposits: distal products of magmatic-hydrothermal systems. Geology 18:157–161

Steele-Maclnnis M (2018) Fluid inclusions in the system H_2O-NaCl-CO_2: an algorithm to determine composition, density and isochore. Che Geol 498:32–44

Sterner SM, Bodnar RJ (1984) Synthetic fluid inclusions in natural quartz I. Compositional types synthesized and applications to experimental geochemistry. Geochim Cosmochim Acta 48:2659

Su WC, Xia B, Zhang HT, Zhang XC, Hu RZ (2008) Visible gold in arsenian pyrite at the Shuiyindong Carlin-type gold deposit, Guizhou, China: implications for the environment and processes of ore formation. Ore Geol Rev 33:667–679

Su WC, Hu RZ, Xia B, Xia Y, Liu YP (2009a) Calcite Sm-Nd isochron age of the Shuiyindong Carlin-type gold deposit, Guizhou, China. Chem Geo 258:269–274

Su WC, Heinrich CA, Pettke T, Zhang XC, Hu RZ, Xia B (2009b) Sediment-hosted gold deposits in Guizhou, China: products of wall-rock sulfidation by deep crustal fluids. Econ Geol 104:73–93

Su WC, Dong WD, Zhang XC, Shen NP, Hu RZ, Hofstra AH, Cheng LZ, Xia Y, Yang KY (2018) Carlin-type gold deposits in the Dian-Qian-Gui "Golden Triangle" of southwest China. Rev Econ Geol 20:157–185

Tan QP, Xia Y, Xie ZJ, Yan J, Wei D (2015a) S, C, O, H, and Pb isotopic studies for the Shuiyindong Carlin-type gold deposit, Southwest Guizhou, China: constraints for ore genesis. Chin J Geochem 34:525–539

Tan QP, Xia Y, Xie ZJ, Yan J (2015b) Migration paths and precipitation mechanisms of ore-forming fluids at the Shuiyindong Carlin-type gold deposit, Guizhou, China. Ore Geol Rev 69:140–156

Tang M, Rudnick RL, Chauvel C (2014) Sedimentary input to the source of Lesser Antilles lavas: a Li perspective. Geochim Cosmochim Acta 144:43–58

Taylor HP (1974) The application of oxygen and hydrogen isotope studies to problems of hydrothermal alteration and ore deposition. Eco Geol 69:843–883

Teng FZ, McDonough WF, Rudnick RL, Dalpe C, Tomascak PB, Chappell BW, Gao S (2004) Lithium isotopic composition and concentration of the upper continental crust. Geochim Cosmochim Acta 68:4167–4178

Teng FZ, McDonough WF, Rudnick RL, Walker RJ (2006a) Diffusion-driven extreme lithium isotopic fractionation in country rocks of the Tin Mountain pegmatite. Earth Planet Sci Lett 243:701–710

Teng FZ, McDonough WF, Rudnick RL, Walker RJ, Sirbescu MLC (2006b) Lithium isotopic systematics of granites and pegmatites from the Black Hills, South Dakota. Am Mineral 91:1488–1498

Tomascak PB, Langmuir CH, le Roux PJ, Shirey SB (2008) Lithium isotopes in global mid-ocean ridge basalts. Geochim Cosmochim Acta 72:1626–1637

Tomascak PB, Magna Tomá, Dohmen R (2016) Lithium in the deep Earth: mantle and crustal systems. In: Advances in Lithium Isotope Geochemistry, Springer, p 119–156

Wang Q, Groves D (2018) Carlin-style gold deposits, Youjiang Basin, China: tectono-thermal and structural analogues of the Carlin-type gold deposits, Nevada, USA. Miner Deposita 53:909–918

Webster JD, Holloway JR, Hervig RL (1989) Partitioning of lithophile trace elements between H_2O and H_2O+CO_2 fluids and topaz rhyolite melt. Eco Geo 84:116–134

Wilkinson J (2001) Fluid inclusions in hydrothermal ore deposits. Lithos 55:229–272

Williams-Jones AE, Palmer DAS (2002) The evolution of aqueous–carbonic fluids in the Amba Dongar carbonatite, India: implications for fenitisation. Chem Geol 185:283–301

Xie ZJ, Xia Y, Cline JS, Pribil MJ, Koenig A, Tan QP, Wei DT, Wang ZP, Yan J (2018) Magmatic origin for sediment-hosted au deposits, Guizhou province, China: in situ chemistry and sulfur isotope composition of pyrites, Shuiyindong and Jinfeng deposits. Econ Geol 113:1627–1652

Xu L, Luo G, Wen HJ, Zhou ZB, Qin CJ (2018) Origin of ore-forming fluids of the Zn-Pb-(Cu) deposits in the Jinbao mine district of eastern Guizhou Province, China: evidence from chemical compositions of fluid inclusions and their lithium isotopes. Geochem J 52:483–496

Xu L, Luo CG, Wen HJ (2020) A revisited purification of Li for 'Na breakthrough' and its isotopic determination by MC-ICP-MS. Geostand Geoanalyt Re 44:201–214

Xu L, Luo CG, Wen HJ, Deng MG, Qin CJ, Zhu CW, Fourestier J (2021) Lithium and chlorine isotopic constraints on fluid sources and evolution at the Luziyuan distal skarn Zn–Pb–Fe–(Cu) deposit, western Yunnan Province, China. Ore Geol Rev 133:104057

Yang J, Cawood PA, Du Y, Huang H, Hu L (2012) Detrital record of Indosinian mountain building in SW China: provenance of the Middle Triassic turbidites in the Youjiang Basin. Tectonophysics 574–575:105–117

Yang D, Hou ZQ, Zhao Y, Hou KJ, Yang ZM, Tian SH, Fu Q (2015) Lithium isotope traces magmatic fluid in a seafloor hydrothermal system. Sci Rep 5:13812

Zhao JH, Zhou MF, Yan DP, Zheng JP, Li JW (2011) Reappraisal of the ages of Neoproterozoic strata in South China: no connection with the Grenvillian orogeny. Geology 39:299–302

Zheng YF (1993) Calculation of oxygen isotope fractionation in hydroxyl-bearing silicates. Eart Planet Sci Lett 120:247–263

Zhu JJ, Hu RZ, Richards JP, Bi XW, Stern R, Lu G (2017) No genetic link between Late Cretaceous felsic dikes and Carlin-type Au deposits in the Youjiang basin, Southwest China. Ore Geol Rev 84:328–337